ACS APPLIED NANO MATERIALS

www.acsanm.org

Article

Insights into the Morphology and Structural Defects of Eu-Doped Ceria Nanostructures for Optoelectronic Applications in Red-Emitting Devices

Pedro Paulo Ortega,* Rafael Aparecido Ciola Amoresi, Marcio Daldin Teodoro, Leonnam Gotardo Merízio, Miguel Angel Ramirez, Celso Manuel Aldao, Cesare Malagù, Miguel Adolfo Ponce, Elson Longo, and Alexandre Zirpoli Simões

Cite This: *ACS Appl. Nano Mater.* 2024, 7, 12466−12479

Read Online

ACCESS | Metrics & More | Article Recommendations | Supporting Information

ABSTRACT: In this work, we investigated the synthesis temperature effect on the crystal growth of Eu-doped ceria nanostructures synthesized via the microwave-assisted hydrothermal method and how it influences their red-light emission. Sphere-like nanoparticles, nanorods, nanorods/nanocubes, and nanocubes were obtained by gradually increasing the synthesis temperature. The structural analysis revealed that the nanocubes displayed higher crystallinity and lower structural disorder in comparison to the other morphologies. X-ray photoelectron spectroscopy (XPS) spectroscopy showed that oxygen vacancies were the predominant defect. The intensity of the photoluminescence emissions of the nanocubes was 60 times higher than that of the sphere-like nanoparticles and nanorods, indicating that the structural symmetry in this morphology is suitable for doping with Eu^{3+}, displaying greater photoluminescence efficiency. The nanocubes also displayed excellent red-light emission, with coordinates (0.63,0.37) close to the red RGB primary at (0.64, 0.32). The lifetime values increased with higher synthesis temperatures. This trend suggests a structural correlation of different morphologies, defects, and homogeneity of the Eu^{3+} distribution in the crystal lattice and the photoluminescence emission and quenching. Therefore, we showed that controlling the morphology of Eu-doped CeO_2 nanostructures is a powerful tool to improve its photoluminescence properties, which is valuable for applications as a red phosphor.

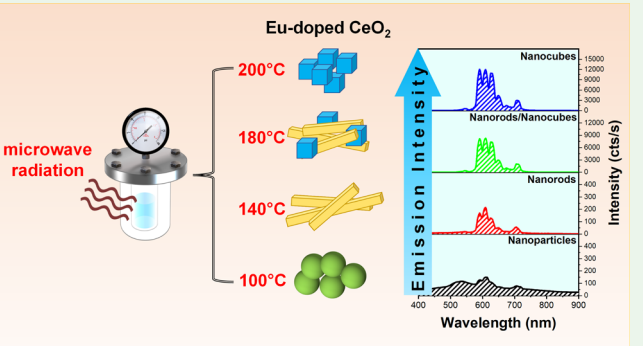

KEYWORDS: *nanostructures, CeO_2, crystal growth, crystal structure, photoluminescence*

1. INTRODUCTION

Solid-state light-emitting materials, such as light-emitting diodes (LEDs), are monochromatic or polychromatic light sources that find diverse applications across residential and commercial lighting, electronic devices, the automotive industry, medical fields, and agriculture.[1] Luminescent materials, commonly referred to as phosphors, can have different compositions, such as $Ca_{1-x-y}Sr_xBa_yAlSiN_3:Eu^{2+}$ and $Ca_{2-x-y}Sr_xBa_ySi_5N_8:Eu^{2+}$, which typically involve expensive precursors and intricate stoichiometries, resulting in a high-cost synthesis process and consequently an expensive final product.[2] Cerium dioxide (CeO_2), or ceria, is an attractive matrix for light-emitting and photoluminescent applications due to its simple stoichiometry and inherent blue emission.[3,4]

Despite numerous studies regarding undoped and doped ceria and their photoluminescence properties, there is still a lack of data on the influence of the crystal growth and morphology of ceria as a light emitter. For instance, as a red-light emitter with a simple stoichiometry and high quantum efficiency, it can be effectively used in LEDs for agricultural applications, aiding in photosynthesis, germination, and overall plant growth.[5] With advancements in solid-state light-emitting technologies, it is imperative to comprehend the behavior of materials within a nanometric scale matrix, characterized by high reactivity and surface energy. This understanding is crucial for achieving high-efficiency emitting devices. This entails, for instance, modifying the nanoparticle morphology and assessing its electronic properties.[6]

Manipulating the morphology of nanomaterials is complex and requires a deep understanding of their growth mechanisms.[7] Thus, choosing an adequate synthesis route is essential

Received: February 11, 2024
Revised: April 16, 2024
Accepted: May 15, 2024
Published: May 22, 2024

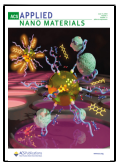

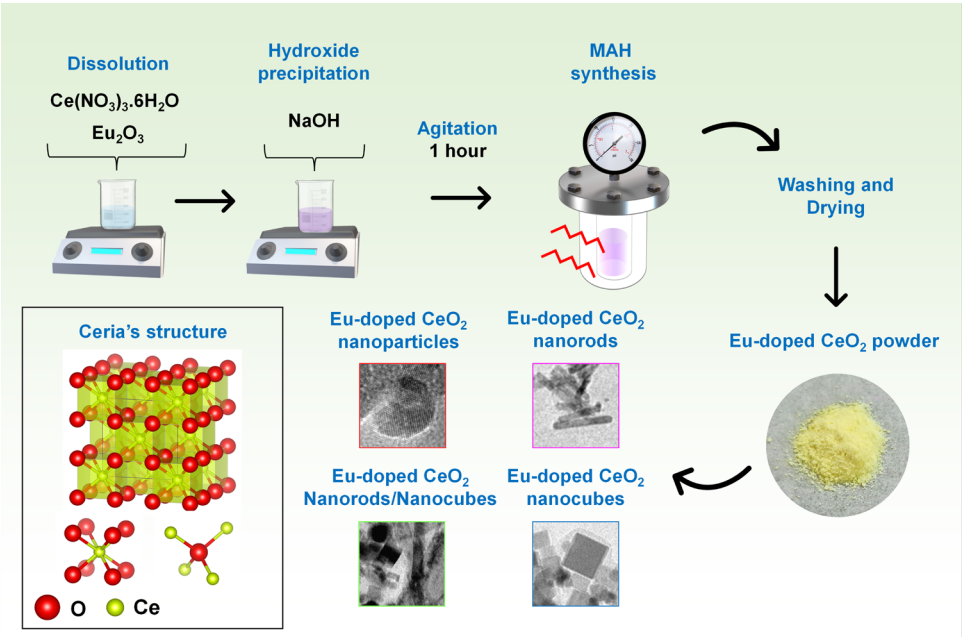

Figure 1. Schematic diagram depicting the synthesis of the Eu-doped ceria nanostructures via the MAH method.

to producing high-quality nanostructures with controlled morphologies. A variety of techniques have been used to prepare ceramic nanostructures, such as coprecipitation,[8] conventional hydrothermal,[9] microwave-assisted hydrothermal,[10] and sol−gel.[11] Among these, the microwave-assisted hydrothermal (MAH) method features a set of advantages over the others, e.g., simplicity, low temperature, short time, and low cost. Also, the MAH synthesis is carried out inside a sealed autoclave, which minimizes the disposal of byproducts into the atmosphere and water systems.[10]

Recently, researchers reported the synthesis of shape-controlled CeO_2 (or ceria) nanostructures using different methodologies,[12−16] but few publications discussed the MAH method.[17,18] Oriented attachment and Ostwald ripening were reported as the main growth mechanisms of ceria nanodisks, nanorods, and nanocubes via wet chemical routes.[9,15] However, the authors used mostly long synthesis time (up to 144 h) or heat treatment at high temperatures (600 °C) to obtain the specific morphologies. In some of these studies, the morphologies are poorly defined or mixed with other shapes. Despite being common in the literature, these results show the complexity involved in synthesizing high-quality nanostructures and indicate the necessity to improve and optimize their synthesis.

Ceria nanostructure has received considerable attention due to its promising applications in gas sensors,[19] solid oxide fuel cells,[20] photocatalysis,[21] and LED components.[22] It is an n-type semiconductor in which the cations of the crystal lattice can easily change their oxidation state from Ce^{4+} to Ce^{3+} (and vice versa) by creating or eliminating oxygen vacancies. By increasing the concentration of oxygen vacancies, electrons initially associated with O 2p states transition to Ce 4f states.[23] As Ce 4f states lie inside the bandgap region of ceria, partially filling Ce 4f states increases the number of carriers and modifies the conductivity of CeO_2.[24] The transitions and nanometric characteristics of CeO_2 particles contribute favorably to the luminescent behavior of this material. Research indicates photoluminescent emission spanning from the ultraviolet[25] to the blue and green range.[26] Doping with rare-earth (RE) elements presents an alternative method for controlling emission properties, such as enhancing intensity or extending emission duration. In this sense, among RE^{3+} cations, Eu^{3+} exhibits intense red photoluminescence emission due to $^5D_0 \rightarrow {}^7F_2$ transitions around 610 nm, thus being used in multiple applications such as glasses, organic and inorganic compounds, polymers, and others.[27−30] Evaluating the production of photoluminescent Eu materials within an oxide matrix, such as CeO_2, offers advantages in practical applications, including enhanced durability, thermal stability, and resistance to corrosive environments. Researchers have attempted to improve the photoluminescence of Eu-doped ceria by changing the dopant concentration, using different codopants, and controlling their microstructure properties.[3,4] For instance, Thorat et al.[31] studied the correlation between the defect chemistry and the photoluminescence properties of Eu-doped ceria nanocrystals, assigning higher emission intensities to higher crystallinity. Furthermore, Eu cations behave as a spectroscopic probe for ceria, providing information regarding the local symmetry at the sites occupied by the dopant cations.

In this work, we investigated how different synthesis temperatures influenced the morphology of europium-doped ceria (CeO_2: 8 wt % Eu) nanostructures prepared using the MAH method. A doping concentration of 8 wt % was selected based on previous results, which indicated that at this concentration, several electronic and electrical properties of ceria, including its photocatalytic and gas sensing properties,[32,33] were improved without the formation of secondary phases. The morphological, structural, and optical properties were analyzed via X-ray diffractometry (XRD), Raman spectroscopy, absorption spectroscopy in the ultraviolet−visible region (UV−vis), photoluminescence emission spectroscopy (PL), transmission electron microscopy (TEM), and X-ray excited photoelectron spectroscopy (XPS). We provided a detailed investigation of the growth mechanisms behind the synthesis of doped ceria nanostructures at different temper-

https://doi.org/10.1021/acsanm.4c00875
ACS Appl. Nano Mater. 2024, 7, 12466−12479

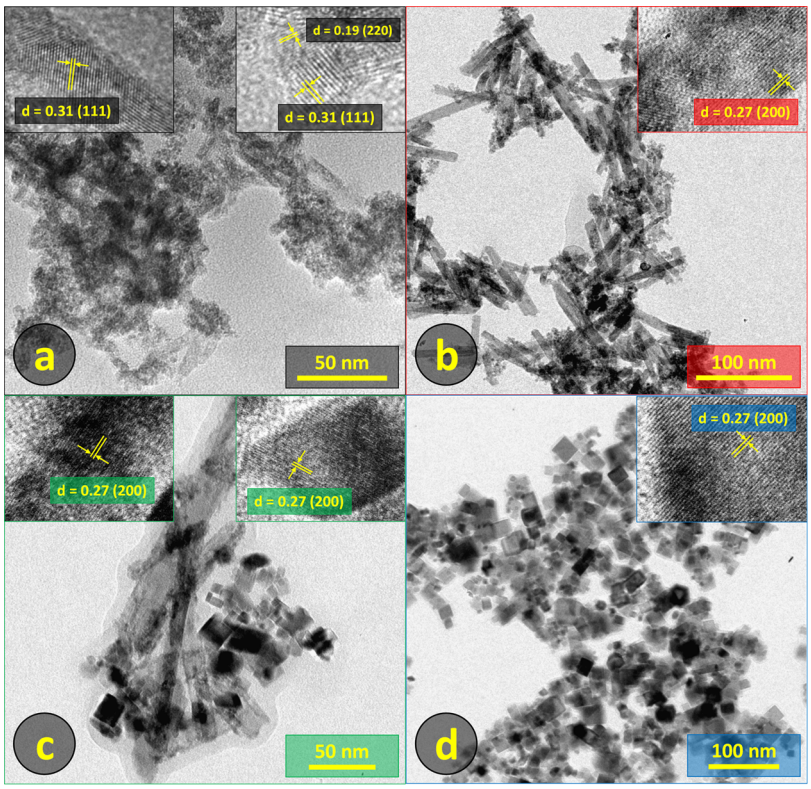

Figure 2. TEM micrographs of the Eu-doped ceria sphere-like nanoparticles (a), nanorods (b), nanorods/nanocubes (c), and nanocubes (d) synthesized via the MAH method at 100, 140, 180, and 200 °C for 8 min, respectively.

atures, and a correlation between crystal growth, morphology, and photoluminescence is established. Therefore, this work provides valuable insights into the synthesis of rare-earth-doped ceria aiming at potentializing their applications in optoelectronic devices.

2. EXPERIMENTAL PROCEDURE

2.1. Synthesis of the Nanostructures. Eu-doped ceria nanostructures (CeO_2: 8 wt % Eu) were synthesized using the microwave-assisted hydrothermal method, as illustrated in Figure 1. First, cerium nitrate hexahydrate ($Ce(NO_3)_3{\cdot}6H_2O$, Sigma-Aldrich) and europium oxide (Eu_2O_3, Sigma-Aldrich) were simultaneously dissolved in distilled water (drops of nitric acid were used to assist in the dissolution of Eu_2O_3). Next, the solutions were mixed under continuous magnetic stirring at room temperature. Subsequently, the mixture was added to a 6 M NaOH (Sigma-Aldrich) solution and homogenized for 1 h. At this stage, a light-purple slurry solution was observed due to the precipitation of Ce and Eu hydroxides. This solution was then transferred into a poly(tetrafluoroethylene) container, sealed, and placed inside a microwave oven (2.45 GHz, 800 W). The synthesis was carried out at 100, 140, 180, and 200 °C for 8 min[34] and corresponded to an autogenous pressure of 98, 294, 490, and 680 kPa, respectively. After the thermal treatment, the system was cooled to room temperature naturally. Finally, the supernatant was collected and washed until the pH was neutralized. The samples were dried overnight at 100 °C. Eu-doped ceria nanostructures were obtained in the form of a light-yellow powder. All reagents used were of analytical grade.

2.2. Characterization of the Nanostructures. The crystalline structure of the nanostructures was investigated in a Rigaku DMax/2500 diffractometer using Cu Kα1 (λ = 1.5406 Å) radiation in the 20−80° range. The Rietveld refinement was performed using GSAS II software over a 10−110° 2θ range collected at 0.02°/min, and the data was fitted based on the face-centered cubic ($Fm\bar{3}m$) structure of CeO_2. Raman spectroscopy was used to analyze the short-range symmetry and presence of structural defects in the samples with a Horiba LabRAM iHR 550 spectrometer using an argon laser (λ = 514 nm) as the excitation source. UV−vis was performed in a PerkinElmer Lambda 1050 spectrophotometer in the 250−2500 nm range using the diffuse reflectance mode. The bandgap energies were estimated by converting the UV−vis data into Tauc plots using the Kubelka−Munk function.[24] The bandgap energy was determined by finding the x-axis coordinate of the point where the extrapolation of the linear portions of the curves intercept. TEM was carried out to study the morphology, exposed planes, and growth mechanisms of the nanostructures. The images were taken at room temperature in a Phillips FEI CM 120 microscope. The room temperature PL spectra were recorded in a detection system composed of a 19.3 spectrometer and a Silicon CCD (Andor−Kymera/Idus) via an excitation laser source emitting at 355 nm (Cobolt/Zouk). Lifetime measurements were conducted utilizing a HORIBA Jobin Yvon Fluorolog 3 spectrofluorometer equipped with a pulsed Xe lamp featuring a 6 μs pulse half-width within a 5.5 ms range and a picosecond photon detector (PPD-850) comprising 4096 channels. Decay curves were acquired with excitation in the $^7F_0 \rightarrow {}^5L_6$ transition and by monitoring the $^5D_0 \rightarrow {}^7F_2$ transition of the Eu^{3+} ion. Lifetime values were derived via second-order exponential decay fitting. XPS was performed to investigate the elemental composition and oxidation states at the surfaces of the Eu-doped nanostructures. The measurements were performed in a Scienta Omicron ESCA+ equipped with a hemispherical analyzer (EA125) with Al Kα ($h\nu$ = 1486.7 eV) as the radiation source. CASA XPS software (Casa Software Ltd., U.K.) was used to analyze the XPS data. The spectra were corrected to the charge effects using the C 1s peak of adventitious carbon at 284.6 eV as a reference. All data processing and fitting of the spectra were based on the correct separation of the doubles and logical sequence of width to half height of the states.

3. RESULTS AND DISCUSSION

3.1. Morphological Analysis. Figure 2 shows the TEM images of the Eu-doped ceria nanostructures synthesized at

https://doi.org/10.1021/acsanm.4c00875
ACS Appl. Nano Mater. 2024, 7, 12466−12479

Table 1. Temperature, Time, Growth-Directing Agents, and Heat Treatment Used in Different Synthesis Methods to Obtain Ceria Nanostructures[a]

synthesis	morphology	temperature	time	growth-driving agents	heat treatment	refs
ME	nanosphere/nanorod	140 °C	12 h	yes	no	12
MAH	nanorod	120 °C	30 min	yes	no	17
CH	nanorod	100 °C	24 h	no	400 °C/4 h	13
	nanocube	180 °C	24 h			
ST	nanocube	180 °C	24 h	yes	no	49
CH	nanocube	150 °C	24 h	no	no	20
CP	nanorod	room temperature	up to 96 h	no	650 °C/6 h	50
SG	spherical	60 °C	2 h	no	500 °C/6 h	51
MASG		130 °C	10 min			
MAH	sphere-like	100 °C	8 min	no	no	this work
	nanorod	140 °C				
	nanocube	200 °C				

[a]ME: microemulsion, MAH: microwave-assisted hydrothermal, CH: conventional hydrothermal, ST: solvothermal, CP: coprecipitation, SG: sol−gel, MASG: microwave-assisted sol−gel.

100, 140, 180, and 200 °C for 8 min via the MAH method. For the synthesis performed at 100 °C (Figure 2a), a mixture of morphologies with poorly defined shapes was observed, most of them sphere-like nanoparticles (4.6 ± 0.3 nm in size), with a few elongated rod-like shapes starting to form. Increasing the synthesis temperature to 140 °C led to the formation of well-defined nanorods (43.8 ± 3.5 in length and 7.4 ± 0.1 in width) though also in an aggregated state (Figure 2b). At 180 °C (Figure 2c), the nanostructures are composed of a mixture of nanorods (48.2 ± 2.0 in length and 12.0 ± 0.5 in width) and nanocubes (14.2 ± 5.3). Finally, at 200 °C (Figure 2d), nanocubes with well-defined shapes and sharp edges were formed (10.1 ± 3.9). At this stage, only nanocubes were observed. Therefore, as the synthesis temperature increased, different exposed crystalline facets were observed, i.e., nanostructures with a change in shape isometry were induced by temperature. The formation of large agglomerates is probably due to the high electron density on the surfaces coming from oxygen vacancy defects. Such phenomenon is common for nanomaterials,[11] and might be avoided by adding surfactants to the synthesis; however, surfactants are known for being growth-directing agents, and as such, their use can influence the final morphology of nanostructures.[35,36] Aggregation of nanoparticles can also be ascribed to van der Waals forces as well as their spontaneous predisposition to form agglomerates to reduce their surface energy. The morphological analysis of Figure 2 (inset boxes depict the interplanar spaces) indicates that, depending on thermodynamic parameters (kinetic energy through temperature), a morphology with a particular exposed surface is consumed by another type of predominant exposed surface: from sphere-like nanoparticles to nanorods to nanocubes. Therefore, except for the sphere-like nanoparticles, which displayed (111) and (110) facets, nanorods and nanocubes exhibited only (100) facets. The same set of exposed facets was reported in the literature for CeO_2 nanorods and nanocubes.[37,38]

To understand the crystal growth mechanisms of specific morphologies, we must consider how the MAH method influences the synthesis. Opposed to most wet synthesis techniques, which usually use conductive heating, the MAH method uses microwave radiation to heat the solution, leading to much higher synthesis rates.[39] The rapid heating results in multiple nucleating sites, which avoid crystal overgrowth and tend to form nanoparticles with an average particle size distribution of as low as 5 nm. Accordingly, we showed in previous works[32,40] that the MAH synthesis of ceria at low temperature (100 °C) and with low OH^- concentration resulted in sphere-like shaped nanoparticles with a reduced average size distribution, and no specific morphologies were identified. However, the sample synthesized at 100 °C and with 6 M NaOH (Figure 2a) showed that rod-like nanostructures started to form (Figure 2a). In this case, rod formation can be explained by the high OH^- concentration used in the synthesis route. Hydroxyls are strong mineralizing agents and cause accelerated crystal growth under high concentrations.[41] The high proportion of mineralizer to metal precursor kinetically favors the growth of facets with higher surface energies, which otherwise would be thermodynamically eliminated, thus inducing the anisotropic growth of crystals in the form of nanorods.[42,43] In such conditions, $Ce(OH)_3$, $Ce(OH)_4$, and $Eu(OH)_3$ precipitates are formed, and $Ce(OH)_3$ is rapidly oxidized to $Ce(OH)_4$.[44] These hydroxides are deprotonated during the synthesis and converted into the Eu-doped ceria nanostructures.[24]

For hydrothermal processes, two mechanisms control the anisotropic growth of nanocrystals: Ostwald ripening and oriented attachment. Depending on the synthesis parameters, one mechanism might prevail over the other or coexist, leading to the growth of different morphologies.[45] As discussed before (Figure 2a), high OH^- concentration, low temperature, and short synthesis time led to mostly sphere-like nanoparticles due to the conversion of small hydroxide aggregates into Eu-doped CeO_2. At this stage, a high number of nucleation sites form in response to the high OH^- concentration in the solution, which increases the contact rate of the nuclei. If the contact between two nuclei occurs via planes with the same crystallographic orientation, they coalesce in a preferable growth direction, forming the nanorods. This mechanism is known as oriented attachment.[46] Increasing the temperature to 140 °C enhances the nuclei collision rate and nanorods with an increased length dominate the final morphology, as shown in Figure 2b. At 180 °C, a mixture of nanorods and nanocubes was observed (Figure 2c), indicating that a different growth mechanism occurs. This shift is confirmed in Figure 2d, where only nanocubes were observed after the synthesis temperature was increased to 200 °C. The well-defined morphology and sharp edges of the nanocubes suggest that Ostwald ripening mechanisms had a greater influence on the crystal growth in

https://doi.org/10.1021/acsanm.4c00875
ACS Appl. Nano Mater. 2024, 7, 12466−12479

higher synthesis temperatures.[44,47] Ostwald ripening is based on dissolution−recrystallization processes, in which small crystals dissolve and recrystallize onto larger particles,[45] forming morphologies with well-defined shapes.[47] Typically, CeO_2 crystals have a low solubility in water, hindering their dissolution−recrystallization processes.[47] Therefore, we suggest that both oriented attachment and Ostwald ripening mechanisms are responsible for the growth of the Eu-doped ceria nanostructures. The former dominates in lower temperatures due to the low solubility of ceria crystals, and the latter becomes gradually more relevant as the synthesis temperature increases (which is possibly ascribed to a higher dissolution−recrystallization promoted by higher temperatures in a concentrated OH^- medium).[47,48]

Table 1 shows the synthesis temperature and time as well as the necessity of growth-directing agents and heat treatment to prepare morphology-specific ceria nanostructures for different synthesis routes. One can observe that the MAH method provides a relatively short temperature and much lower synthesis time to obtain the morphologies. Moreover, since no postheat treatment and growth-driving agents were needed, the synthesis routine is simpler, cost-effective, and environment-friendly, being appropriate for large-scale production.

Despite being scarce, some studies have shown the influence of the system's pressure on the crystal formation under hydrothermal conditions. Demoisson et al.[52] have shown that the synthesis of ZnO at low temperatures and low pressures leads to the presence of zinc hydroxide intermediary products in the samples. At room temperature, increasing the pressure resulted mostly in intermediary products. The authors also observed that an increasing temperature resulted in a pure ZnO phase. Another study has shown that increasing the pressure at high temperatures improves sample crystallinity.[53] These results are similar to the ones observed in this work: low temperatures and pressures (the pressure is autogenous) resulted in samples with lower crystallinities (sphere-like nanoparticles and nanorods), and higher temperatures and pressures led to samples with better crystallinities, as shown in the Section 3.2. The pressure also increases the reaction rate and might lead to smaller nanostructures, though their effect in morphology seems less significant than time and temperature.[52]

3.2. Structural Analysis. The XRD patterns of the Eu-doped ceria sphere-like nanoparticles, nanorods, nanorods/nanocubes, and nanocubes are shown in Figure 3. Based on the ICSD file #239412, we indexed all of the reflections to ceria's cubic fluorite phase ($Fm\bar{3}m$ space group), except for the sphere-like nanoparticles. As shown in Figure S2, the additional three small reflections were assigned to $Ce(OH)_3$, which is an intermediary product formed during the addition of the precursor solution into the concentrated OH solution.[54] The presence of $Ce(OH)_3$ indicates that the temperature or time used to prepare the sphere-like nanoparticles (100 °C for 8 min, with 6 M NaOH) did not provide enough energy to fully convert the $Ce(OH)_3$ products into CeO_2 crystals. Some studies have shown that the hydrothermal synthesis performed at low temperatures and pressures resulted in the presence of intermediary products in the samples.[52] In previous works, we have found syntheses at 100 °C for 8 min to be sufficient to completely convert $Ce(OH)_3$ into CeO_2 nanoparticles;[24,34,55] however, in those works, a much lower OH^- concentration was used, which, in turn, might lead to a lower concentration of $Ce(OH)_3$ products and result in their complete conversion

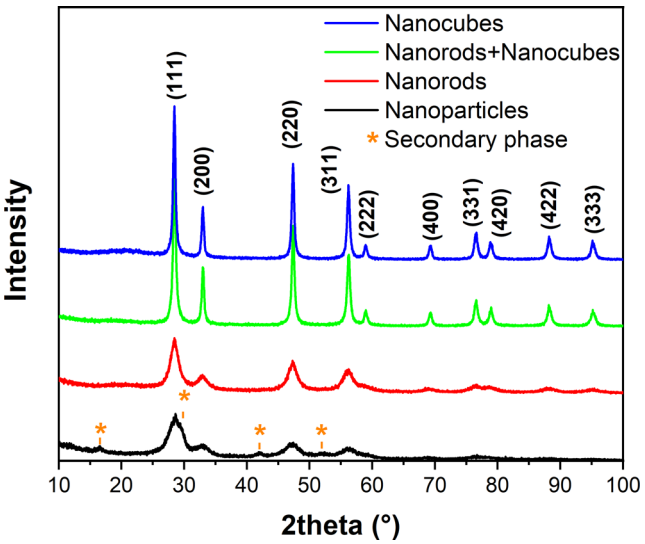

Figure 3. XRD pattern of the Eu-doped ceria sphere-like nanoparticles, nanorods, nanorods/nanocubes, and nanocubes synthesized via the MAH method at 100, 140, 180, and 200 °C, for 8 min, respectively. The asterisk (*) indicates the hydroxide phase.

into CeO_2 crystals. The absence of reflections related to secondary phases or impurities in the other samples indicates the formation of a solid solution upon doping with Eu. The higher crystallinity of the nanorods/nanocubes and nanocubes, which were synthesized at higher temperatures, corroborates with the analysis of crystal growth mechanisms discussed in Section 3.1 since Ostwald ripening is associated with an increase in crystallinity.[47] Also, it is well known that the size distribution of nanoparticles directly influences the peak broadening in the XRD pattern.[56] Thus, the reduced size of the nanoparticles (4.6 nm) and nanorods (7.4 nm in width), as shown in Figure S1 and Table S1, can explain the larger peak broadening observed for these samples. Rietveld refinement analysis (Figure S2 and Table S2) revealed a decrease in lattice microstrain with an increasing synthesis temperature. This suggests that lower synthesis temperatures, in combination with high mineralizer concentration and short reaction time, lead to higher concentrations of structural defects and lattice distortions.[47] The lattice parameter agrees with the values reported in the literature for CeO_2,[57] and the fitting parameters indicate that the data obtained from the refinement analysis are reliable.

Raman spectroscopy was employed to analyze the phase formation, short-range order−disorder, and structural defects of the samples (Figure 4). The crystal lattice of pure CeO_2 displays one vibrational mode around 465 cm^{-1}, which is assigned to the symmetric stretching of oxygen atoms in the $[CeO_8]$ clusters (F_{2g} mode).[58] As shown in Figure 4, the presence of an intense Raman mode around 460 cm^{-1} confirms the formation of ceria's fluorite-type cubic phase for all samples. Raman spectroscopy accounts for the short-range order of the structure, being complementary to the XRD analysis (which probes the long-range order of crystalline samples). Therefore, Raman analysis proved the formation of the fluorite-type phase for the sphere-like nanoparticles despite their long-range periodicity not being highly crystalline, especially compared with the nanocubes and nanorods/nanocubes. No modes associated with precursors or intermediary products (e.g., Eu_2O_3 would display a vibrational mode at

https://doi.org/10.1021/acsanm.4c00875
ACS Appl. Nano Mater. 2024, 7, 12466−12479

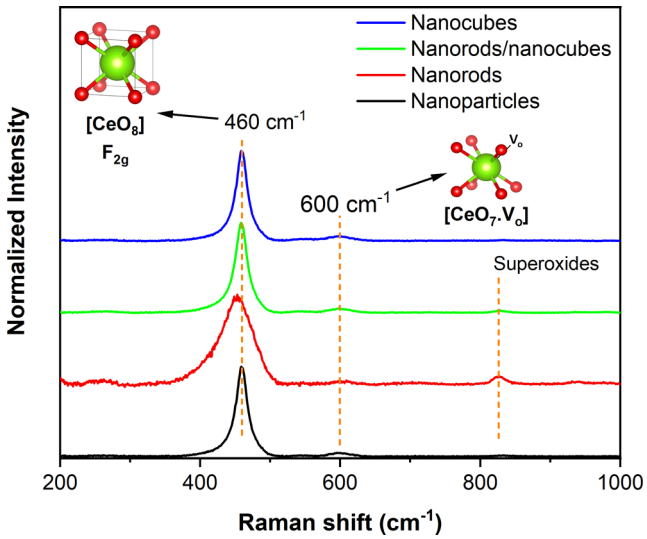

Figure 4. Raman spectra of the Eu-doped ceria sphere-like nanoparticles, nanorods, nanorods/nanocubes, and nanocubes synthesized via the MAH method at 100, 140, 180, and 200 °C for 8 min, respectively.

337 cm^{-1}[59]) were found, reinforcing that the samples are crystalline and without secondary phases. The nanorods and nanorods/nanocubes also displayed a weak mode attributed to adsorbed superoxides around 830 cm^{-1},[60] which might be related to the exposed facet type.

The $[CeO_8]$ clusters are sensitive to changes in the oxygen sublattice, providing valuable information about the short-range order−disorder and structural defects. Dopant Eu^{3+} cations have a lower oxidation state and a larger ionic radius when compared with host Ce^{4+} cations (Eu^{3+} = 1.066 Å and Ce^{4+} = 0.97 Å), causing distortions in the structure when used as a CeO_2 dopant. These distortions result in a slight blue shift in the F_{2g} mode for the Eu-doped samples,[61] suggesting a certain degree of order−disorder in the structure.[62] Table S3 shows the F_{2g} mode position and full width at half-minimum (fwhm) values for each sample.

Nanorods displayed the highest shift for the F_{2g} mode compared with the single crystal (465 cm^{-1}), indicating a higher degree of structural disorders. The estimated fwhm values corroborate this statement: the F_{2g} mode of the nanorods is broader and asymmetric, which is associated with a decrease in the short-range symmetry and the nanometric scale of the samples.[61] The opposite was observed for the nanocubes. Therefore, the morphology of the samples influences the short-range order−disorder of the nanostructures. Also, structural disorders are associated with a transverse optical mode around 260 cm^{-1}, which was observed only for the nanorods.[63] Two primary sources contribute to the origin of oxygen vacancies in our samples: the replacement of Ce^{4+} cations for Eu^{3+} and the reduction of Ce^{4+} to Ce^{3+}. In both processes, due to charge differences between Eu^{3+} or Ce^{3+} and Ce^{4+}, a displacement of the Fermi level in relation to the conduction and valence bands occurs, resulting in the formation of oxygen vacancies, which can be seen as a weak Raman mode around 600 cm^{-1}.[64]

The elemental composition and oxidation states of the samples were analyzed by XPS, as shown in Figure 5. The photoemission peaks referring to the presence of the elements Ce, O, and Eu as the constituents of the material are evident in the survey spectra (Figure 5i). It is observed that the atomic composition of europium on the surface is between 2.0 and 2.3% (which corresponds to Eu-doping percentages between ~6.6 and ~7.5 mol %), as expected from the doping carried out in the synthesis. Figure 5ii illustrates the O 1s spectra. For the sphere-like nanoparticles (Figure 5ii-a), the spectrum was fitted with four peaks: ~ 529, ~531, ~533, and ~535 eV. The peak at ~529 eV was attributed to Ce−O bonds in the lattice. The peak at ~531 eV is associated with water molecules or hydroxide species that are chemisorbed onto the surface of the nanostructures.[65,66] Since the chemisorption of these species is associated with defective sites on the surface, the peak at ~531 eV can be associated with surface defects (in this case, oxygen vacancies (V_O)). The peaks at ~533 and 535 eV are related to carbon−oxygen bond species (C−O, C═O) and nitrogen−oxygen bond species (N−O), respectively.[67] The photoemission peak of the N−O bond is observed only for the sphere-like nanoparticles, probably a result of the low crystallinity of the sample arising from the precursors and low synthesis temperature. Differences in the photoemission area associated with oxygen bound to Ce (~529 eV, Ce−O) and surface defects (~531 eV, V_o) are observed among the samples. It is verified that at higher synthesis temperatures, there is a lower ratio between defects and O−Ce (V_o/O−Ce data shown in Figure 5ii).

Similarly, a correlation is found in the spectra obtained for the photoemission of Ce 3d (Figure 5iii). In this figure, the spectra were fitted with Ce^{3+} species, denoted as v_0/u_0 and v′/u′, which refer to primary photoemission from Ce^{3+} and its shakedown, respectively, and Ce^{4+}, denoted as v/u, v″/u″ and v‴/u‴, referring to the primary photoemission from Ce^{4+} and its shakedown features, respectively. The notations v and u are related to the spin−orbit coupling of $3d_{5/2}$ and $3d_{3/2}$, respectively.[68,69] It is observed from the area ratio corresponding to each oxidation state (%Ce^{3+} = (area Ce^{3+}/(area Ce^{3+} + area Ce^{4+})) × 100%) that, at higher synthesis temperatures, there is a lower predominance of Ce^{3+} species, in agreement with the lower concentration of defects obtained in the O 1s results. The Eu 4d spectra (Figure 5iv) agree with Eu^{3+} species.[70]

Therefore, increasing the synthesis temperature does not change the oxidation state of the dopant element but completely changes the defect states and concentration of the Ce^{3+} species. Such facts are associated with the morphologies and the main exposed surfaces. In the case of the syntheses at lower temperatures, sphere-like nanoparticles and nanorods present a predominance of surfaces (111) and (220), while the syntheses at higher temperatures lead to a predominance of surfaces (200) for the nanorods/nanocubes and nanocubes. Computer simulations[42] reveal that different surfaces display different $[CeO_x]$ clusters with the respective oxygen vacancy species determined by the surface termination, that is, the surface planes (111), (220), and (200) display clusters of the type $[CeO_7].V_o^z$, $[CeO_6]{\cdot}2V_o^z$, and $[CeO_6]{\cdot}V_o^z$, respectively. Thus, the relationship between the morphologies obtained and the concentration of defects correlates with the type of surface exposed in the nanostructures. Other parameters that might influence the defect structure are the crystallinity and the structural disorder level of the samples.

3.3. Optical Analysis. Figure 6 shows the estimated bandgap energies (E_{gap}) for the Eu-doped ceria nanostructures. The E_{gap} predicted theoretically for CeO_2 is around 6 eV (corresponding to the difference between O 2p and Ce 5d

https://doi.org/10.1021/acsanm.4c00875
ACS Appl. Nano Mater. 2024, 7, 12466−12479

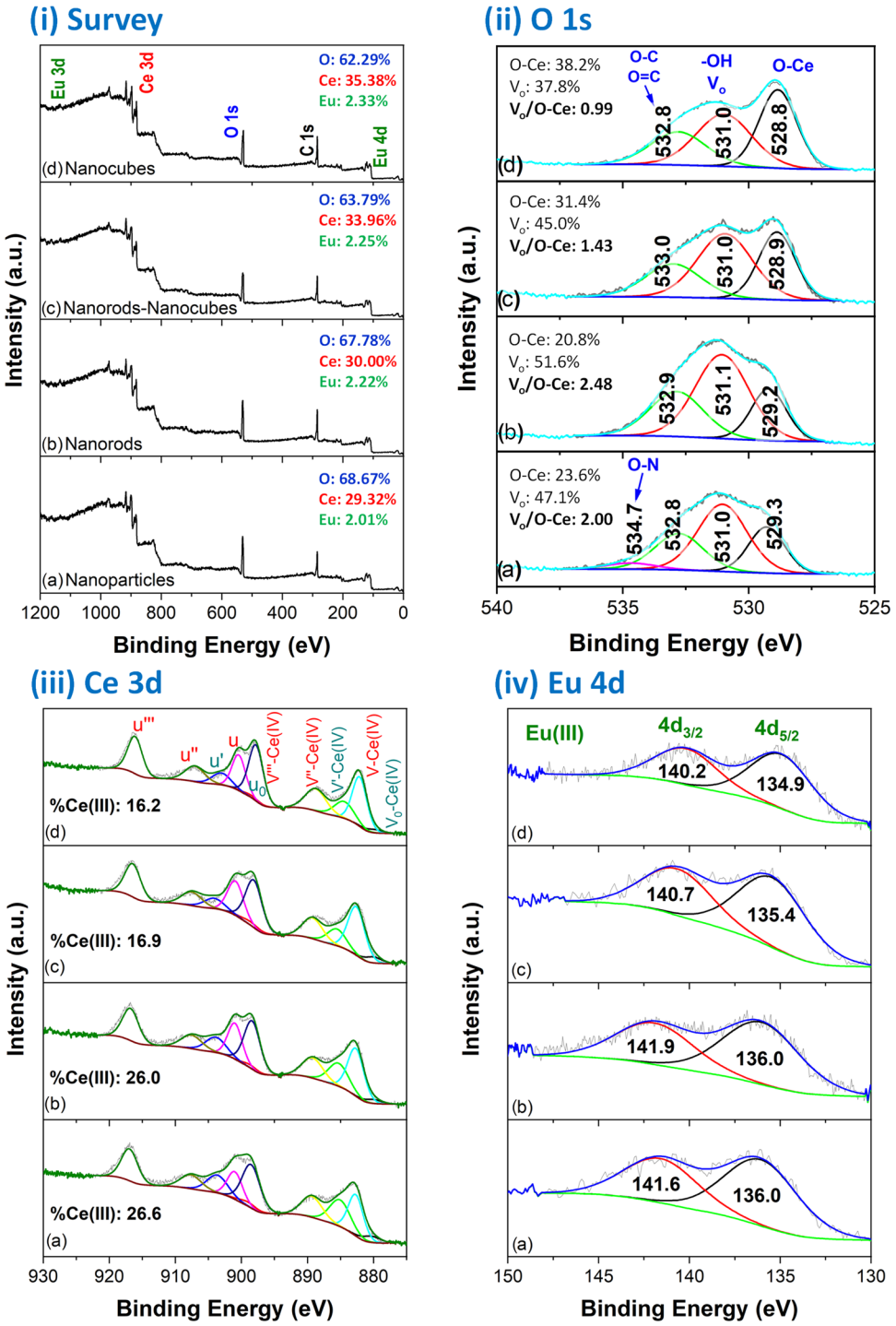

Figure 5. Survey spectra (i) and high-resolution XPS for the O 1s (ii), Ce 3d (iii), and Eu 4d (iv) species for the Eu-doped ceria sphere-like nanoparticles (a), nanorods (b), nanorods/nanocubes (c), and nanocubes (d) synthesized via the MAH method at 100, 140, 180, and 200 °C for 8 min.

states), but the E_{gap} usually observed experimentally is lower (approximately 3 eV) due to Ce 4f states located inside the bandgap. That is, these states behave as a conduction band, and increasing their occupancy increases the conductivity of the samples via hopping conduction mechanisms. According to the literature, doping ceria can shift the edges of the conduction and valence bands, which results in a decrease or increase in the bandgap energy depending on the doping element.[71,72] Accordingly, the E_{gap} obtained for the Eu-doped ceria samples in Figure 6 is lower than the values reported in the literature for pure ceria nanostructures.[15,61] The E_{gap} varied from 2.35 eV for the nanorods to 2.64 eV for the nanocubes and is consistent with the values reported for rare-earth-doped ceria.[73,74] In the nanorods/nanocubes sample, it is possible to infer two contributions with bandgap energies of 2.17 and 2.51 eV. This fact refers to the presence of the two morphologies (nanorods and nanocubes) found in the sample. Each morphology has its respective surfaces and surface terminations, which results in different defect densities and, consequently, different bandgap energies.[75] The lowest E_{gap}

https://doi.org/10.1021/acsanm.4c00875
ACS Appl. Nano Mater. 2024, 7, 12466−12479

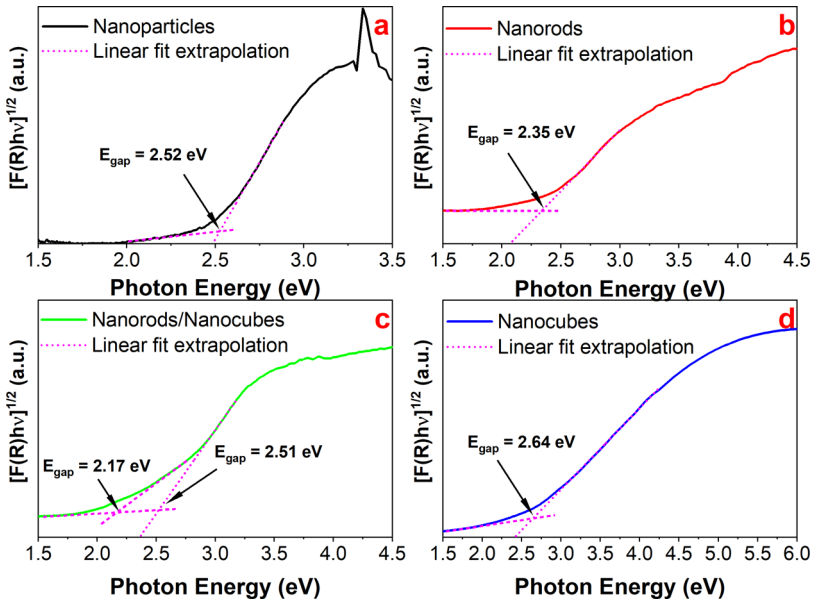

Figure 6. Tauc plots and bandgap energies (E_{gap}) of the Eu-doped ceria sphere-like nanoparticles (a), nanorods (b), nanorods/nanocubes (c), and nanocubes (d) synthesized via the MAH method at 100, 140, 180, and 200 °C for 8 min, respectively.

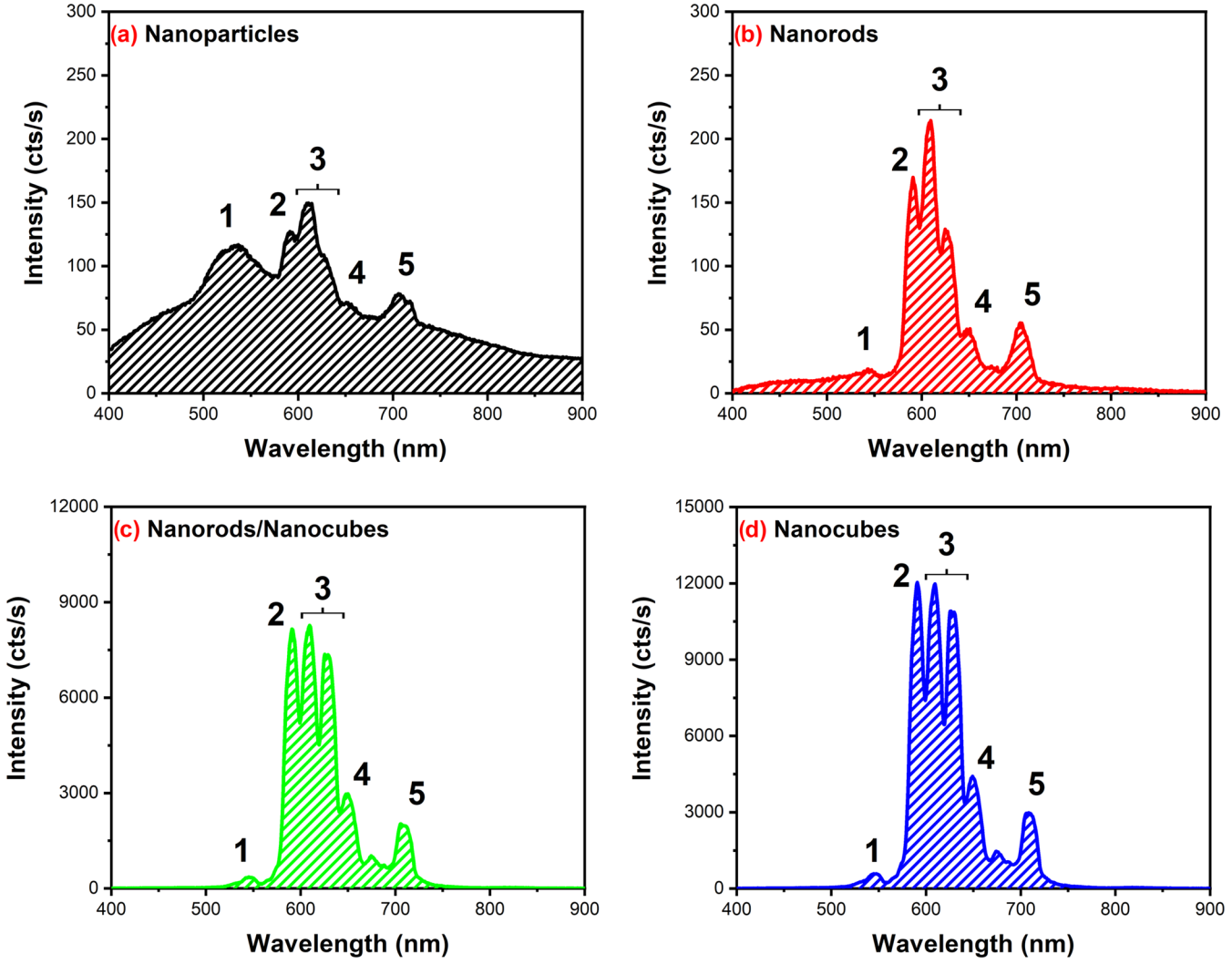

Figure 7. Photoluminescence spectra of the Eu-doped ceria: (a) sphere-like nanoparticles, (b) nanorods, (c) nanorods/nanocubes, and (d) nanocubes synthesized via the MAH method at 100, 140, 180, and 200 °C for 8 min, respectively. Excitation source, λ_{exc} = 355 nm.

https://doi.org/10.1021/acsanm.4c00875
ACS Appl. Nano Mater. 2024, 7, 12466−12479

value observed for the nanorods might be explained by its higher structural disorder level (discussed in the Raman analysis), and it is corroborated by the XPS analysis, which shows an increased number of Ce^{3+} for the sphere-like and nanorod morphologies. It is worth mentioning that previous studies[42,47] associated small variations in the E_{gap} of pure ceria nanostructures with their different morphologies, suggesting that the exposed facets of each morphology influence the E_{gap} value.

The photoluminescence emissions of the Eu-doped ceria nanostructures are shown in Figure 7. Before the emission spectra of the samples are analyzed, it is important to understand the photoluminescence behavior of undoped CeO_2. As discussed previously, in ceria-based compounds, oxygen vacancies are created by intrinsic (nonstoichiometry) and extrinsic (doping) mechanisms. Each oxygen vacancy (V_O) leaves behind an electron pair that localizes near the vacancy in Ce 4f states and forms $Ce^{3+} - V_O - Ce^{3+}$ complexes, which are the most stable defect in the ceria structure.[76] However, electrons can also be trapped in the vacancy site, forming mono- or doubly ionized oxygen vacancies. Then, three types of F centers can be created depending on their ionization: F^0, F^+, and F^{+2} for neutral, mono ($V_O^{\bullet}$), and doubly ($V_O^{\bullet\bullet}$) ionized oxygen vacancies, respectively. As proposed by Radović et al.,[77] these F centers are localized between Ce $4f^0$ and Ce $4f^1$ states and directly influence the band structure and magnetic and optical properties of CeO_2. The authors also showed that F centers may not form for all CeO_2 nanostructures and are highly dependent on the synthesis method. Therefore, complexes such as $Ce^{3+} - V_O - Ce^{3+}$, $Ce^{4+} - V_O^{\bullet} - Ce^{3+}$, and $Ce^{4+} - V_O^{\bullet\bullet} - Ce^{4+}$ promote electronic transitions that usually result in a broad and low-intensity emission in the blue-green region of the photoluminescence spectra of pure ceria, as reported in the literature.[78,79]

Electronic transitions in europium cations lead to intense photoluminescence emissions, making the emission spectra of Eu-doped samples significantly different from those of pure ceria. As shown in Figure 7, the Eu-doped ceria nanostructures show well-defined, high-intensity bands, especially for rod/cube and cube morphologies (Figure 7c,d, respectively). Europium cations (Eu^{3+}) have the electronic configuration of xenon atoms plus 6 electrons in 4f shells (represented by [Xe] $4f^6$). This configuration allows multiple intraconfigurational f–f electronic transitions between Eu^{3+} energy levels, but the most relevant for the photoluminescence emissions are between ^5D (excited) and ^7F (ground) energy levels, specifically $^5D_0 \rightarrow {}^7F_J$ (J = 0, 1, 2, 3, 4, 5, 6), as shown in Figure S3.[80] Each electronic transition appears in the spectra at the following wavelengths: 545 nm ($^5D_0 \rightarrow {}^7F_0$), 590 nm ($^5D_0 \rightarrow {}^7F_1$), 610 and 630 nm ($^5D_0 \rightarrow {}^7F_2$), 650 nm ($^5D_0 \rightarrow {}^7F_3$), and 710 nm ($^5D_0 \rightarrow {}^7F_4$). As reported by Binnemans,[81] these transitions have characteristics (such as nondegeneracy of $^5D_0$ and $^7F_0$ states, no overlap between emission lines, and high-intensity emissions) that make Eu^{3+} cations an interesting spectroscopic probe for local symmetry of the matrix structure.

The presence of $^5D_0 \rightarrow {}^7F_0$ transitions (band 1) and the high intensity of $^5D_0 \rightarrow {}^7F_1$ (band 2) indicate that Eu^{3+} replaces preferentially Ce^{4+} sites in the lattice.[81,82] The $^5D_0 \rightarrow {}^7F_1$ transitions are associated with magnetic dipole transitions and therefore are not affected by the crystal field around Eu^{3+}. Conversely, $^5D_0 \rightarrow {}^7F_2$ (band 3) transitions around 610 and 630 nm are attributed to electric dipole transitions and are hypersensitive to the crystal field around sites occupied by Eu^{3+}.[81] As proposed by Liu et al.[82] and Tanner,[83] if the emission intensity of $^5D_0 \rightarrow {}^7F_2$ transitions is higher than those of $^5D_0 \rightarrow {}^7F_1$, i.e., $I(^5D_0 \rightarrow {}^7F_2) > I(^5D_0 \rightarrow {}^7F_1)$, there is a symmetry distortion around Eu^{3+} sites. That is true for the photoluminescence spectra of the sphere-like nanoparticles (Figure 7a) and the nanorods (Figure 7b), suggesting a higher local distortion when compared with the nanorods/nanocubes and nanocubes. Moreover, broader and less intense bands were observed for the sphere-like nanoparticles and nanorods (especially the nanoparticles), indicating these samples present a higher structural disorder level. This analysis agrees with the structural discussion performed in Section 3.2, in which it was shown by Raman analyses that the nanorods exhibited a broader and asymmetric band, indicating a greater disorder in the system. Such disorder results in a heterogeneous dispersion of Eu^{3+} ions in the crystal lattice, creating an emission trapping state,[84,85] and thus a lower photoluminescence intensity was observed for the nanorods. Likewise, sphere-like nanoparticles have a higher density of defects, as discussed in the XPS analysis. These defects indirectly contribute to the heterogeneity of the Eu^{3+} distribution and result in an emission quenching effect.[86]

Another interesting observation that supports the findings is how the emission transitions correlate with crystalline symmetry. In the ceria fluorite structure, the sites occupied by Ce^{4+} cations exhibit O_h symmetry and are coordinated by eight oxygen anions; therefore, these sites possess an inversion center.[82] Literature shows that sites with inversion centers do not allow electric dipole transitions for Eu^{3+}.[87] However, in this work, we show that doping the structure and the environment in which this doping occurs (morphology) create oxygen vacancies to compensate for the charge difference between Ce^{4+} and Eu^{3+}, which introduces symmetry distortions that end up allowing electric dipole transitions, resulting in $^5D_0 \rightarrow {}^7F_3$ (band 4 at ∼650 nm) and $^5D_0 \rightarrow {}^7F_4$ (band 5 at ∼710 nm) transitions,[81] as observed in Figure 7. Bands 4 and 5 are usually weak but sensitive to symmetry distortions. Here, again, we observe that for the sphere-like nanoparticles and nanorods, the emission intensities of $^5D_0 \rightarrow {}^7F_3$ and $^5D_0 \rightarrow {}^7F_4$ are weaker compared with the other morphologies, indicating that defects present in these structures are symmetrically unfavorable for dipole transitions and prevent greater photoluminescence efficiency. Transitions from $^5D_0$ to $^7F_5$ and $^7F_6$ levels would appear around 750 and 820 nm, respectively, but these transitions are very weak and generally not detected in photoluminescence investigations.[81]

Based on the photoluminescence emission of the nanostructures, we also investigated their color emission using the chromaticity diagram (CIE 1931, *Commision Internationale de l'Eclairage*) shown in Figure 8. The color emission regions for each nanostructure were yellow-orange (sphere-like nanoparticles), orange-red (nanorods), and red (nanorods/nanocubes and nanocubes). In fact, the red emission of the nanorods/nanocubes and nanocubes are centered at (0.62,0.37) and (0.63,0.37) coordinates, respectively, which are very close to the red RGB primary at (0.64,0.32).[88] These results agree with the studies of Singh et al.,[89] in which the authors reported red-light emission for Eu-doped ceria nanoparticles synthesized via a sol–gel-assisted combustion route. The literature shows several photoluminescent ceria nanostructures, but few experimentally evaluate the radioactive lifetime of ceria samples doped with Eu or altered morphology.

https://doi.org/10.1021/acsanm.4c00875
ACS Appl. Nano Mater. 2024, 7, 12466−12479

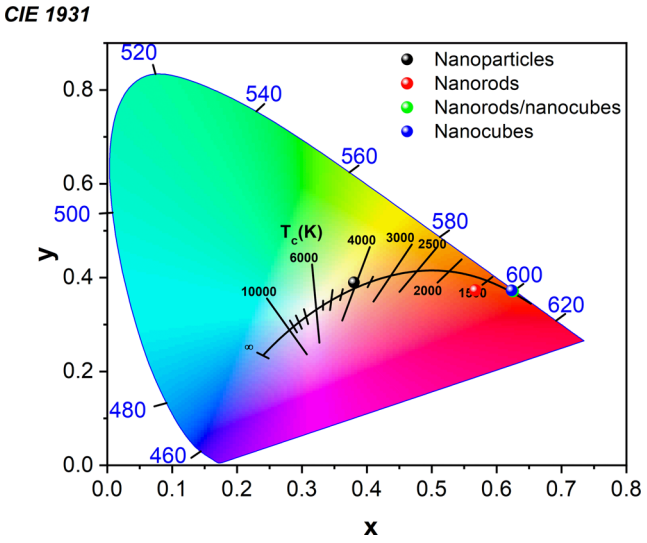

Figure 8. CIE 1931 chromaticity diagram and color emission of the Eu-doped ceria nanostructures synthesized via the MAH method.

Radiative lifetime is an important factor in the energy efficiency and performance of LED materials. Thus, given the photoluminescent properties of Eu^{3+} ions, the lifetime measurements shown in Figure 9 provide valuable information about the emission process. This figure illustrates the lifetime decay curves obtained by directly exciting the samples in the $^7F_0 \rightarrow {}^5L_6$ (396 nm) transition and monitoring the $^5D_0 \rightarrow {}^7F_2$ (610 nm) transition of Eu^{3+} ions. The observed lifetime curves exhibit nonlinear decay, resulting in multiple lifetime values. This phenomenon was expected, given the nanometric dimensions of the particles.

Thus, the decay curves were fitted by using a second-order exponential function, and the average lifetime (τ_{avg}) was calculated according to eq 1. Table 2 summarizes the lifetime value of the samples, and Figure S3 provides the fitting parameters.

$$\tau_{avg} = \frac{\sum_i A_i \tau_i^2}{\sum_i A_i \tau_i} \quad (1)$$

The τ_{avg} represents the average decay lifetime, τ_1 and τ_2 are the decay lifetime obtained by the fitting, and A_1 and A_2 are constants. Similarly to what was observed in the emission spectra, there is an increase in the average lifetime value for samples with higher synthesis temperatures. As discussed before, the increase in the synthesis temperature changes the morphology due to different crystal growth mechanisms. For lower temperatures, it is observed that small particles with spherical shapes were formed. Spherical particles usually exhibit a higher surface area, allowing for more Eu^{3+} ions to be exposed at the surface. Consequently, the lifetime has a strong contribution of nonradiative loss mechanisms, meaning

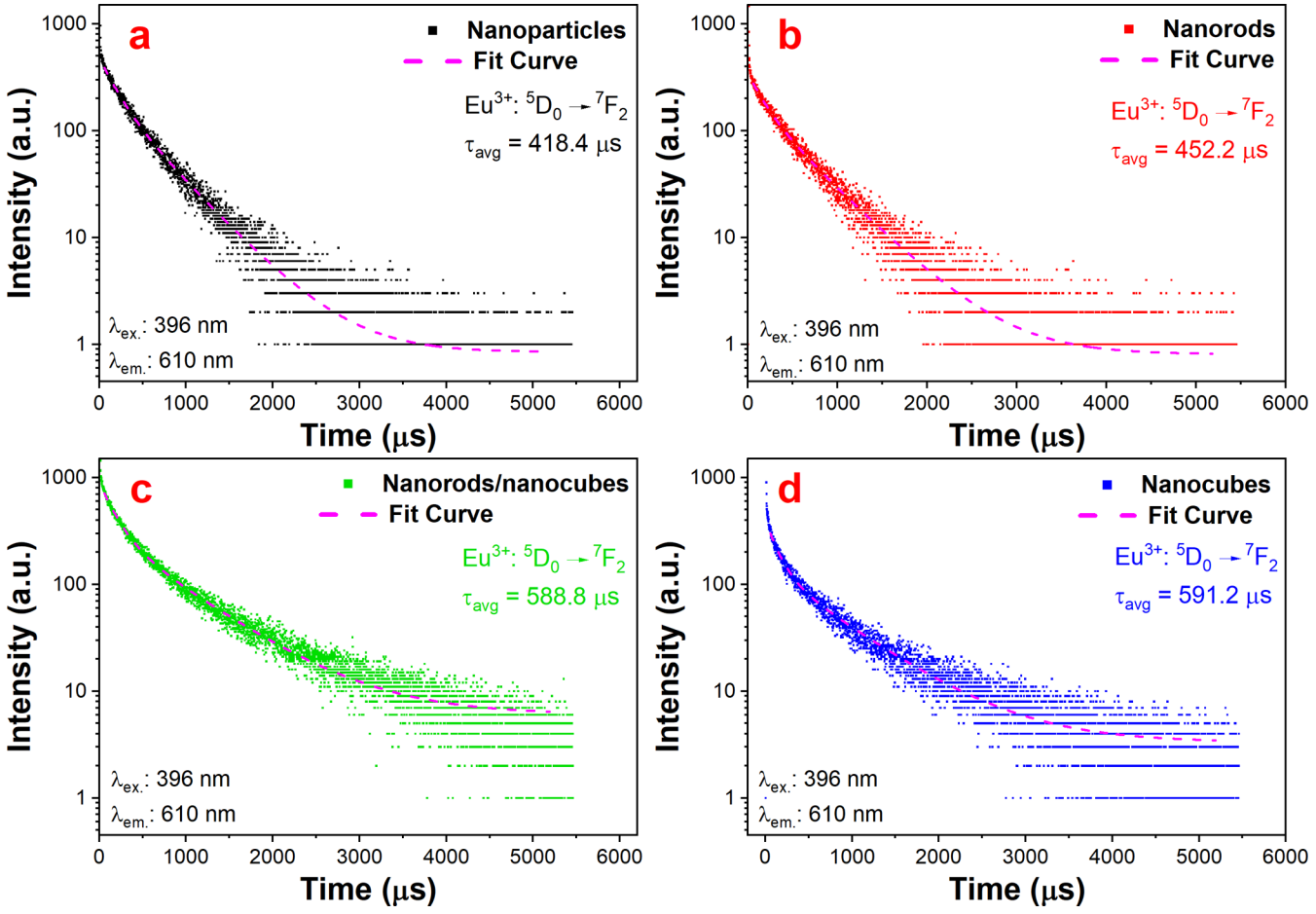

Figure 9. Lifetime decay curves of the Eu-doped ceria sphere-like nanoparticles (a), nanorods (b), nanorods/nanocubes (c), and nanocubes (d) synthesized via the MAH method at 100, 140, 180, and 200 °C for 8 min, respectively.

https://doi.org/10.1021/acsanm.4c00875
ACS Appl. Nano Mater. 2024, 7, 12466−12479

Table 2. Lifetime Decay Values of the Eu-Doped Ceria Sphere-like Nanoparticles, Nanorods, Nanorods/Nanocubes, and Nanocubes Synthesized via the MAH Method at 100, 140, 180, and 200 °C for 8 min

sample	A_1	τ_1 (μs)	A_2	τ_2 (μs)	τ_{avg} (μs)	R^2
nanoparticles	256.9	177.9	229.5	511.9	418.4	0.993
nanorods	160.2	164.7	184.6	529.7	452.2	0.990
nanorods/nanocubes	597.3	169.3	312.9	765.8	588.8	0.995
nanocubes	266.3	131.9	138.6	747.1	591.2	0.986

a shorter lifetime.[90,91] For the nanorods, the increased defect density amplifies the heterogeneity in the dispersion of europium ions within the lattice, thereby contributing to nonradiative decay processes. When the synthesis temperature is increased to 180 °C, nanocubes start to be formed with higher crystallinity and size, leading to an increase in the lifetime value. Finally, only nanocubes are observed for the synthesis performed at 200 °C, meaning that the nanorods and small nanoparticles are no longer influencing the Eu^{3+} ions lifetime, leading to an increase in the average lifetime value.[91,92] Therefore, doping ceria with Eu^{3+} cations and controlling their growth mechanisms are promising alternatives to developing red-light components for LED applications.

4. CONCLUSIONS

In this work, we have synthesized Eu-doped ceria nanostructures (CeO_2: 8 wt % Eu) via the microwave-assisted hydrothermal method. Sphere-like nanoparticles, nanorods, and nanocubes were obtained as the synthesis temperature was increased from 100 to 200 °C. Different sets of exposed facets ((111), (220), and (200)) were observed for each morphology. Based on their TEM micrographs, oriented attachment and Ostwald ripening were suggested as the growth mechanisms, with Ostwald ripening dominating at higher synthesis temperatures. The structural analysis revealed that the ceria fluorite cubic phase was formed for all samples. However, the samples synthesized at lower temperatures (sphere-like nanoparticles and nanorods) presented a higher structural disorder level and minimal amounts of nitrate groups on their surface. Raman and XPS analyses revealed distinct chemical environments within each morphology, indicating that nanoparticles with spherical and nanorod shapes exhibit a higher proportion of defects and disorder compared to nanocubes. These factors significantly impact the even distribution of Eu^{3+} ions throughout the crystal lattice. The photoluminescence emissions due to europium F centers showed that a higher structural disorder level for the sphere-like nanoparticles and nanorods results in emission trapping sites, reducing the photoluminescence efficiency of these samples. The color emissions for each nanostructure were yellow-orange (sphere-like nanoparticles), orange-red (nanorods), and red (nanorods/nanocubes and nanocubes). Excellent red-light emission was observed for the nanocubes, with coordinates (0.63,0.37) close to the red RGB primary at (0.64, 0.32). The lifetime measurements aligned with the proposed growth theory, as higher lifetime values were achieved with an increased synthesis temperature. This suggests that the chemical environment, symmetry, and defects present in each morphology are decisive for the dispersion of Eu^{3+} ions over the crystal lattice, consequently minimizing nonradiative decays. Therefore, doping ceria with Eu^{3+} cations and controlling their growth mechanisms is a promising alternative to improve their applicability in multiple research fields such as gas sensors, photocatalysis, and LED components.

■ ASSOCIATED CONTENT

Supporting Information

The Supporting Information is available free of charge at https://pubs.acs.org/doi/10.1021/acsanm.4c00875.

Average particle size distribution; Rietveld refinement results of the Eu-doped CeO_2 nanostructures; peak position and fwhm data from Raman spectroscopy analysis; intraconfigurational f−f electronic transitions of europium cations; and data obtained from radiative decay time curve fits (PDF)

■ AUTHOR INFORMATION

Corresponding Author

Pedro Paulo Ortega − *School of Engineering of Guaratinguetá, São Paulo State University (UNESP), Guaratinguetá 12516-410, Brazil; Federal University of São Carlos (UFSCar), São Carlos 13565-905, Brazil;* orcid.org/0000-0002-4254-1281; Email: pedro.ortega@unesp.br

Authors

Rafael Aparecido Ciola Amoresi − *School of Engineering of Guaratinguetá, São Paulo State University (UNESP), Guaratinguetá 12516-410, Brazil; Center for Engineering, Modeling and Applied Social Sciences, Federal University of ABC (UFABC), Santo André 09210-580, Brazil;* orcid.org/0000-0002-7523-6013

Marcio Daldin Teodoro − *Federal University of São Carlos (UFSCar), São Carlos 13565-905, Brazil*

Leonnam Gotardo Merízio − *São Carlos Institute of Physics (IFSC), University of São Paulo (USP), São Carlos 13560-970, Brazil;* orcid.org/0000-0001-6153-1903

Miguel Angel Ramirez − *School of Engineering of Guaratinguetá, São Paulo State University (UNESP), Guaratinguetá 12516-410, Brazil*

Celso Manuel Aldao − *Institute of Scientific and Technological Research in Electronics (ICYTE), National Research Council (CONICET), University of Mar del Plata (UNMdP), Mar del Plata B7600, Argentina*

Cesare Malagù − *Department of Physics and Earth Sciences, University of Ferrara (UNIFE), Ferrara 44122, Italy;* orcid.org/0000-0002-8362-5289

Miguel Adolfo Ponce − *Physics and Engineering Research Center CIFICEN (UNCPBA-CICPBA-CONICET), Tandil B7000GHG, Argentina*

Elson Longo − *Federal University of São Carlos (UFSCar), São Carlos 13565-905, Brazil;* orcid.org/0000-0001-8062-7791

Alexandre Zirpoli Simões − *School of Engineering of Guaratinguetá, São Paulo State University (UNESP), Guaratinguetá 12516-410, Brazil*

https://doi.org/10.1021/acsanm.4c00875
ACS Appl. Nano Mater. 2024, 7, 12466−12479

Complete contact information is available at:
https://pubs.acs.org/10.1021/acsanm.4c00875

Funding

The Article Processing Charge for the publication of this research was funded by the Coordination for the Improvement of Higher Education Personnel - CAPES (ROR identifier: 00x0ma614).

Notes

The authors declare no competing financial interest.

■ ACKNOWLEDGMENTS

The authors gratefully acknowledge the financial support of the São Paulo State Research Foundation (FAPESP) to the development of this work, process numbers 2021/10780-0, 2018/26550-0, 2017/19143-7, 2023/07486-8, 2019/21770-5, and 2013/07296-2 (CEPID/CDMF).

■ REFERENCES

(1) Cho, J.; Park, J. H.; Kim, J. K.; Schubert, E. F. White Light-Emitting Diodes: History, Progress, and Future. *Laser Photonics Rev.* **2017**, *11* (2), No. 1600147.

(2) Gai, S.; Zhu, H.; Gao, P.; Zhou, C.; Kong, Z.; Molokeev, M. S.; Qi, Z.; Zhou, Z.; Xia, M. Structure Analysis, Tuning Photoluminescence and Enhancing Thermal Stability on Mn^{4+}-Doped $La_{2-X}Y_xMgTiO_6$ Red Phosphor for Agricultural Lighting. *Ceram. Int.* **2020**, *46* (12), 20173−20182.

(3) Raj, A. K. V.; Rao, P. P.; Sreena, T. S.; Thara, T. R. A. Influence of Local Structure on Photoluminescence Properties of Eu^{3+} Doped CeO_2 Red Phosphors through Induced Oxygen Vacancies by Contrasting Rare Earth Substitutions. *Phys. Chem. Chem. Phys.* **2017**, *19* (30), 20110−20120.

(4) Sahoo, S. K.; Mohapatra, M.; Anand, S. Characterization and Optical Properties of Eu-Doped Cubic Nano Ceria Synthesized by Using the Co-Precipitation-Hydrothermal Route. *J. Korean Phys. Soc.* **2013**, *62* (2), 297−304.

(5) Huang, X.; Guo, H. Finding a Novel Highly Efficient Mn4+-Activated $Ca_3La_2W_2O_{12}$ Far-Red Emitting Phosphor with Excellent Responsiveness to Phytochrome PFR: Towards Indoor Plant Cultivation Application. *Dye. Pigm.* **2018**, *152*, 36−42.

(6) Zhou, N.; Liu, L.; Zhou, Z.; Zhang, Y.; Li, M.; Zhou, C.; Xia, M.; Zhou, Z. Engineering Cation Vacancies to Improve the Luminescence Properties of $Ca_{14}Al_{10}Zn_6O_{35}$: Mn^{4+} Phosphors for LED Plant Lamp. *J. Am. Ceram. Soc.* **2020**, *103* (3), 1798−1808.

(7) Rafique, M.; Tahir, M. B.; Rafique, M. S.; Safdar, N.; Tahir, R.Nanostructure Materials and Their Classification by Dimensionality. In *Nanotechnology and Photocatalysis for Environmental Applications*; Elsevier, 2020; pp 27−44.

(8) Zhang, Z.; Wang, Y.; Lu, J.; Zhang, J.; Li, M.; Liu, X.; Wang, F. Pr-Doped CeO_2 Catalyst in the Prins Condensation-Hydrolysis Reaction: Are All of the Defect Sites Catalytically Active? *ACS Catal.* **2018**, *8* (4), 2635−2644.

(9) Yan, L.; Yu, R.; Chen, J.; Xing, X. Template-Free Hydrothermal Synthesis of CeO_2 Nano-Octahedrons and Nanorods: Investigation of the Morphology Evolution. *Cryst. Growth Des.* **2008**, *8* (5), 1474−1477.

(10) Ortega, P. P.; Silva, C. C.; Ramirez, M. A.; Biasotto, G.; Foschini, C. R.; Simões, A. Z. Multifunctional Environmental Applications of ZnO Nanostructures Synthesized by the Microwave-Assisted Hydrothermal Technique. *Appl. Surf. Sci.* **2021**, *542*, No. 148723.

(11) Fudala, A. S.; Salih, W. M.; Alkazaz, F. F. Synthesis Different Sizes of Cerium Oxide CeO_2 Nanoparticles by Using Different Concentrations of Precursor via Sol−Gel Method. *Mater. Today Proc.* **2022**, *49*, 2786−2792.

(12) Huang, Y.; Cai, Y.; Qiao, D.; Liu, H. Morphology-Controllable Synthesis and Characterization of CeO_2 Nanocrystals. *Particuology* **2011**, *9* (2), 170−173.

(13) Hu, J.; Wu, B.; Chen, L.; Song, C.; Yang, H.; Long, F.; Sun, J.; Chi, R. Influences of CeO_2 Morphology on Enhanced Performance of Electro-Fenton for Wastewater Treatment. *J. Rare Earths* **2022**, *40*, 1870−1877.

(14) Fauzi, A. A.; Jalil, A. A.; Hassan, N. S.; Aziz, F. F. A.; Azami, M. S.; Hussain, I.; Saravanan, R.; Vo, D.-V. N. A Critical Review on Relationship of CeO_2-Based Photocatalyst towards Mechanistic Degradation of Organic Pollutant. *Chemosphere* **2022**, *286*, No. 131651.

(15) Mousavi-Kamazani, M.; Azizi, F. Facile Sonochemical Synthesis of Cu Doped CeO_2 Nanostructures as a Novel Dual-Functional Photocatalytic Adsorbent. *Ultrason. Sonochem.* **2019**, *58*, No. 104695.

(16) Choudhary, S.; Sahu, K.; Bisht, A.; Singhal, R.; Mohapatra, S. Template-Free and Surfactant-Free Synthesis of CeO_2 Nanodiscs with Enhanced Photocatalytic Activity. *Appl. Surf. Sci.* **2020**, *503*, No. 144102.

(17) Phuruangrat, A.; Thongtem, T.; Thongtem, S. Effect of NaOH on Morphologies and Photocatalytic Activities of CeO_2 Synthesized by Microwave-Assisted Hydrothermal Method. *Mater. Lett.* **2017**, *193*, 161−164.

(18) Alhumaimess, M.; Aldosari, O.; Alshammari, H.; Kamel, M. M.; Betiha, M. A.; Hassan, H. M. A. Ionic Liquid Green Synthesis of CeO_2 Nanorods and Nano-Cubes: Investigation of the Shape Dependent on Catalytic Performance. *J. Mol. Liq.* **2019**, *279*, 649−656.

(19) Deus, R. C.; Amoresi, R. A. C.; Desimone, P. M.; Schipani, F.; Rocha, L. S. R.; Ponce, M. A.; Simoes, A. Z.; Longo, E. Electrical Behavior of Cerium Dioxide Films Exposed to Different Gases Atmospheres. *Ceram. Int.* **2016**, *42* (13), 15023−15029.

(20) Li, L.; Zhu, B.; Zhang, J.; Yan, C.; Wu, Y. Electrical Properties of Nanocube CeO_2 in Advanced Solid Oxide Fuel Cells. *Int. J. Hydrogen Energy* **2018**, *43* (28), 12909−12916.

(21) Santiago, A. A. G.; Neto, N. F. A.; Longo, E.; Paskocimas, C. A.; Motta, F. V.; Bomio, M. R. D. Fast and Continuous Obtaining of Eu^{3+} Doped CeO_2 Microspheres by Ultrasonic Spray Pyrolysis: Characterization and Photocatalytic Activity. *J. Mater. Sci. Mater. Electron.* **2019**, *30* (12), 11508−11519.

(22) Rajesh, K.; Sakthivel, P.; Santhanam, A.; Venugobal, J. Incorporation of Silver Ion on Structural and Optical Characteristics of CeO_2 Nanoparticles: White LED Applications. *Optik* **2020**, *216*, No. 164800.

(23) Skorodumova, N. V.; Simak, S. I.; Lundqvist, B. I.; Abrikosov, I. A.; Johansson, B. Quantum Origin of the Oxygen Storage Capability of Ceria. *Phys. Rev. Lett.* **2002**, *89* (16), No. 166601.

(24) Ortega, P. P.; Hangai, B.; Moreno, H.; Rocha, L. S. R.; Ramírez, M. A.; Ponce, M. A.; Longo, E.; Simões, A. Z. Tuning Structural, Optical, and Gas Sensing Properties of Ceria-Based Materials by Rare-Earth Doping. *J. Alloys Compd.* **2021**, *888*, No. 161517.

(25) Sun, C.; Li, H.; Zhang, H.; Wang, Z.; Chen, L. Controlled Synthesis of CeO_2 Nanorods by a Solvothermal Method. *Nanotechnology* **2005**, *16* (9), No. 1454.

(26) Wang, G.; Mu, Q.; Chen, T.; Wang, Y. Synthesis, Characterization and Photoluminescence of CeO_2 Nanoparticles by a Facile Method at Room Temperature. *J. Alloys Compd.* **2010**, *493* (1−2), 202−207.

(27) Kitagawa, Y.; Wada, S.; Islam, M. D. J.; Saita, K.; Gon, M.; Fushimi, K.; Tanaka, K.; Maeda, S.; Hasegawa, Y. Chiral Lanthanide Lumino-Glass for a Circularly Polarized Light Security Device. *Commun. Chem.* **2020**, *3* (1), No. 119.

(28) Yawalkar, M. M.; Nair, G. B.; Zade, G. D.; Dhoble, S. J. Effect of the Synthesis Route on the Luminescence Properties of Eu^{3+} Activated $Li_6M(BO_3)_3$ (M = Y, Gd) Phosphors. *Mater. Chem. Phys.* **2017**, *189*, 136−145.

(29) Niu, P.; Liu, X.; Wang, Y.; Zhao, W. Photoluminescence Properties of a Novel Red-Emitting Phosphor $Ba_2LaV_3O_{11}$:Eu^{3+}. *J. Mater. Sci. Mater. Electron.* **2018**, *29* (1), 124−129.

(30) Zhao, J.; Gao, H.; Xu, H.; Zhao, Z.; Bu, H.; Cao, X.; He, L.; Yang, Z.; Sun, J. Structure and Photoluminescence of Eu^{3+} Doped Sr_2InTaO_6 Red Phosphor with High Color Purity. *RSC Adv.* **2021**, *11* (14), 8282−8289.
(31) Thorat, A. V.; Ghoshal, T.; Carolan, P.; Holmes, J. D.; Morris, M. A. Defect Chemistry and Vacancy Concentration of Luminescent Europium Doped Ceria Nanoparticles by the Solvothermal Method. *J. Phys. Chem. C* **2014**, *118* (20), 10700−10710.
(32) Ortega, P. P.; Rocha, L. S. R.; Cortés, J. A.; Ramirez, M. A.; Buono, C.; Ponce, M. A.; Simões, A. Z. Towards Carbon Monoxide Sensors Based on Europium Doped Cerium Dioxide. *Appl. Surf. Sci.* **2019**, *464*, 692−699.
(33) Ortega, P. P.; Amoresi, R. A. C.; Teodoro, M. D.; Longo, E.; Ponce, M. A.; Simões, A. Z. Relationship among Morphology, Photoluminescence Emission, and Photocatalytic Activity of Eu-Doped Ceria Nanostructures: A Surface-Type Effect. *Ceram. Int.* **2023**, *49* (13), 21411−21421.
(34) Deus, R. C.; Foschini, C. R.; Spitova, B.; Moura, F.; Longo, E.; Simões, A. Z. Effect of Soaking Time on the Photoluminescence Properties of Cerium Oxide Nanoparticles. *Ceram. Int.* **2014**, 1−9.
(35) Taniguchi, T.; Watanabe, T.; Sakamoto, N.; Matsushita, N.; Yoshimura, M. Aqueous Route to Size-Controlled and Doped Organophilic Ceria Nanocrystals. *Cryst. Growth Des.* **2008**, *8* (10), 3725−3730.
(36) Makinose, Y.; Taniguchi, T.; Katsumata, K. I.; Okada, K.; Matsushita, N. Facet Control of Ceria Nanocrystals Synthesized by an Oleate-Modified Hydrothermal Method. *Adv. Powder Technol.* **2016**, *27* (1), 64−71.
(37) He, L.; Ren, Y.; Fu, Y.; Yue, B.; Tsang, S. C. E.; He, H. Morphology-Dependent Catalytic Activity of Ru/CeO_2 in Dry Reforming of Methane. *Molecules* **2019**, *24* (3), No. 526.
(38) Gawade, P.; Mirkelamoglu, B.; Ozkan, U. S. The Role of Support Morphology and Impregnation Medium on the Water Gas Shift Activity of Ceria-Supported Copper Catalysts. *J. Phys. Chem. C* **2010**, *114* (42), 18173−18181.
(39) Mirzaei, A.; Neri, G. Microwave-Assisted Synthesis of Metal Oxide Nanostructures for Gas Sensing Application: A Review. *Sens. Actuators, B* **2016**, 749−775.
(40) Cabral, A. C.; Cavalcante, L. S.; Deus, R. C.; Longo, E.; Simões, A. Z.; Moura, F. Photoluminescence Properties of Praseodymium Doped Cerium Oxide Nanocrystals. *Ceram. Int.* **2014**, *40* (3), 4445−4453.
(41) Byrappa, K.; Yoshimura, M.*Handbook of Hydrothermal Technology*, 2nd ed.; Elsevier, 2013.
(42) Amoresi, R. A. C.; Oliveira, R. C.; Marana, N. L.; De Almeida, P. B.; Prata, P. S.; Zaghete, M. A.; Longo, E.; Sambrano, J. R.; Simões, A. Z. CeO_2 Nanoparticle Morphologies and Their Corresponding Crystalline Planes for the Photocatalytic Degradation of Organic Pollutants. *ACS Appl. Nano Mater.* **2019**, *2* (10), 6513−6526.
(43) Burton, W. K.; Cabrera, N.; Frank, F. C. The Growth of Crystals and the Equilibrium Structure of Their Surfaces. *Philos. Trans. R. Soc. London Ser. A,: Math. Phys. Eng. Sci.* **1951**, *243* (866), 299−358.
(44) Lin, M.; Fu, Z. Y.; Tan, H. R.; Tan, J. P. Y.; Ng, S. C.; Teo, E. Hydrothermal Synthesis of CeO_2 Nanocrystals: Ostwald Ripening or Oriented Attachment? *Cryst. Growth Des.* **2012**, *12* (6), 3296−3303.
(45) Chen, G.; Xu, C.; Song, X.; Xu, S.; Ding, Y.; Sun, S. Template-Free Synthesis of Single-Crystalline-like CeO_2 Hollow Nanocubes. *Cryst. Growth Des.* **2008**, *8* (12), 4449−4453.
(46) Godinho, M.; Ribeiro, C.; Longo, E.; Leite, E. R. Influence of Microwave Heating on the Growth of Gadolinium-Doped Cerium Oxide Nanorods. *Cryst. Growth Des.* **2008**, *8* (2), 384−386.
(47) de Oliveira, R. C.; Amoresi, R. A. C.; Marana, N. L.; Zaghete, M. A.; Ponce, M.; Chiquito, A. J.; Sambrano, J. R.; Longo, E.; Simões, A. Z. Influence of Synthesis Time on the Morphology and Properties of CeO_2 Nanoparticles: An Experimental−Theoretical Study. *Cryst. Growth Des.* **2020**, *20* (8), 5031−5042.
(48) Mai, H. X.; Sun, L. D.; Zhang, Y. W.; Si, R.; Feng, W.; Zhang, H. P.; Liu, H. C.; Yan, C. H. Shape-Selective Synthesis and Oxygen Storage Behavior of Ceria Nanopolyhedra, Nanorods, and Nanocubes. *J. Phys. Chem. B* **2005**, *109* (51), 24380−24385.
(49) Qian, L.; Zhu, J.; Du, W.; Qian, X. Solvothermal Synthesis, Electrochemical and Photocatalytic Properties of Monodispersed CeO_2 Nanocubes. *Mater. Chem. Phys.* **2009**, *115* (2−3), 835−840.
(50) Wang, Z.; Xin, Y.; Zhang, Z.; Li, Q.; Zhang, Y.; Zhou, L. Synthesis of Fe-Doped CeO_2 Nanorods by a Widely Applicable Coprecipitation Route. *Chem. Eng. J.* **2011**, *178*, 436−442.
(51) Polychronopoulou, K.; Zedan, A. F.; Katsiotis, M. S.; Baker, M. A.; AlKhoori, A. A.; AlQaradawi, S. Y.; Hinder, S. J.; AlHassan, S. Rapid Microwave Assisted Sol-Gel Synthesis of CeO_2 and $Ce_xSm_{1-X}O_2$ Nanoparticle Catalysts for CO Oxidation. *Mol. Catal.* **2017**, *428*, 41−55.
(52) Demoisson, F.; Piolet, R.; Bernard, F. Hydrothermal Synthesis of ZnO Crystals from $Zn(OH)_2$ Metastable Phases at Room to Supercritical Conditions. *Cryst. Growth Des.* **2014**, *14* (11), 5388−5396.
(53) Liu, W.; Wang, S.; Wang, J.; Zhang, B.; Liu, L.; Liu, H.; Yang, J. Supercritical Hydrothermal Synthesis of Nano-Zinc Oxide: Process and Mechanism. *Ceram. Int.* **2022**, *48* (16), 22629−22646.
(54) Yamaguchi, I.; Watanabe, M.; Shinagawa, T.; Chigane, M.; Inaba, M.; Tasaka, A.; Izaki, M. Preparation of Core/Shell and Hollow Nanostructures of Cerium Oxide by Electrodeposition on a Polystyrene Sphere Template. *ACS Appl. Mater. Interfaces* **2009**, *1* (5), 1070−1075.
(55) Deus, R. C.; Cilense, M.; Foschini, C. R.; Ramirez, M. A.; Longo, E.; Simões, A. Z. Influence of Mineralizer Agents on the Growth of Crystalline CeO_2 Nanospheres by the Microwave-Hydrothermal Method. *J. Alloys Compd.* **2013**, 245−251.
(56) Holder, C. F.; Schaak, R. E. Tutorial on Powder X-Ray Diffraction for Characterizing Nanoscale Materials. *ACS Nano* **2019**, *13* (7), 7359−7365.
(57) Carregosa, J. D. C.; Grilo, J. P. F.; Godoi, G. S.; Macedo, D. A.; Nascimento, R. M.; Oliveira, R. M. P. B. Microwave-Assisted Hydrothermal Synthesis of Ceria (CeO_2): Microstructure, Sinterability and Electrical Properties. *Ceram. Int.* **2020**, *46* (14), 23271−23275.
(58) Tiwari, S.; Rathore, G.; Patra, N.; Yadav, A. K.; Bhattacharya, D.; Jha, S. N.; Tseng, C. M.; Liu, S. W.; Biring, S.; Sen, S. Oxygen and Cerium Defects Mediated Changes in Structural, Optical and Photoluminescence Properties of Ni Substituted CeO_2. *J. Alloys Compd.* **2019**, *782*, 689−698.
(59) Yu, Z.; Wang, Q.; Ma, Y.; Wang, L. X-Ray Diffraction and Spectroscopy Study of Nano-Eu_2O_3 structural Transformation under High Pressure. *J. Alloys Compd.* **2017**, *701*, 542−548.
(60) Schilling, C.; Hofmann, A.; Hess, C.; Ganduglia-Pirovano, M. V. Raman Spectra of Polycrystalline CeO_2: A Density Functional Theory Study. *J. Phys. Chem. C* **2017**, *121* (38), 20834−20849.
(61) Alla, S. K.; Komarala, E. V. P.; Mandal, R. K.; Prasad, N. K. Structural, Optical and Magnetic Properties of Cr-Substituted CeO_2 Nanoparticles. *Mater. Chem. Phys.* **2016**, *182*, 280−286.
(62) Dong, F.; Meng, Y.; Han, W.; Zhao, H.; Tang, Z. Morphology Effects on Surface Chemical Properties and Lattice Defects of Cu/CeO_2 Catalysts Applied for Low-Temperature CO Oxidation. *Sci. Rep.* **2019**, *9* (1), No. 12056.
(63) Gong, J.; Meng, F.; Yang, X.; Fan, Z.; Li, H. Controlled Hydrothermal Synthesis of Triangular CeO_2 nanosheets and Their Formation Mechanism and Optical Properties. *J. Alloys Compd.* **2016**, *689*, 606−616.
(64) Quan, Y. H.; Miao, C.; Li, T.; Wang, N.; Wu, M. M.; Zhang, N.; Zhao, J. X.; Ren, J. Effect of Preparation Methods on the Structure and Catalytic Performance of CeO_2 for Toluene Combustion. *J. Fuel Chem. Technol.* **2021**, *49* (2), 211−219.
(65) Ye, K.; Li, K.; Lu, Y.; Guo, Z.; Ni, N.; Liu, H.; Huang, Y.; Ji, H.; Wang, P. An Overview of Advanced Methods for the Characterization of Oxygen Vacancies in Materials. *TrAC Trends Anal. Chem.* **2019**, *116*, 102−108.
(66) Fan, W.; Li, H.; Zhao, F.; Xiao, X.; Huang, Y.; Ji, H.; Tong, Y. Boosting the Photocatalytic Performance of (001) BiOI: Enhancing

https://doi.org/10.1021/acsanm.4c00875
ACS Appl. Nano Mater. 2024, 7, 12466−12479

Donor Density and Separation Efficiency of Photogenerated Electrons and Holes. *Chem. Commun.* **2016**, *52* (30), 5316−5319.
(67) Chen, F.; Ho, P.; Ran, R.; Chen, W.; Si, Z.; Wu, X.; Weng, D.; Huang, Z.; Lee, C. Synergistic Effect of CeO_2 Modified TiO_2 Photocatalyst on the Enhancement of Visible Light Photocatalytic Performance. *J. Alloys Compd.* **2017**, *714*, 560−566.
(68) Mullins, D. R.; Overbury, S. H.; Huntley, D. R. Electron Spectroscopy of Single Crystal and Polycrystalline Cerium Oxide Surfaces. *Surf. Sci.* **1998**, *409* (2), 307−319.
(69) Reddy, B. M.; Khan, A.; Yamada, Y.; Kobayashi, T.; Loridant, S.; Volta, J. C. Surface Characterization of CeO_2/SiO_2 and $V_2O_5/CeO_2/SiO_2$ Catalysts by Raman, XPS, and Other Techniques. *J. Phys. Chem. B* **2002**, *106* (42), 10964−10972.
(70) Baltrus, J. P.; Keller, M. J. Rare Earth Oxides Eu_2O_3 and Nd_2O_3 Analyzed by XPS. *Surf. Sci. Spectra* **2019**, *26* (1), No. 014001.
(71) Kumari, K.; Aljawfi, R. N.; Chawla, A. K.; Kumar, R.; Alvi, P. A.; Alshoaibi, A.; Vij, A.; Ahmed, F.; Abu-samak, M.; Kumar, S. Engineering the Optical Properties of Cu Doped CeO_2 NCs for Application in White LED. *Ceram. Int.* **2020**, *46* (6), 7482−7488.
(72) Sonsupap, S.; Waehayee, A.; Siritanon, T.; Saenrang, W.; Chanlek, N.; Nakajima, H.; Rattanachata, A.; Maensiri, S. Structural, Optical, and Photocatalytic Properties of La3+ Doped CeO_2 Nanospheres for Enhanced Photodegradation of Tetracycline. *Colloids Surf., A* **2023**, *659*, No. 130650.
(73) Zhu, C.; Wei, X.; Li, W.; Pu, Y.; Sun, J.; Tang, K.; Wan, H.; Ge, C.; Zou, W.; Dong, L. Crystal-Plane Effects of CeO_2 {110} and CeO_2 {100} on Photocatalytic CO2 Reduction: Synergistic Interactions of Oxygen Defects and Hydroxyl Groups. *ACS Sustainable Chem. Eng.* **2020**, *8* (38), 14397−14406.
(74) Lei, W.; Zhang, T.; Gu, L.; Liu, P.; Rodriguez, J. A.; Liu, G.; Liu, M. Surface-Structure Sensitivity of CeO_2 Nanocrystals in Photocatalysis and Enhancing the Reactivity with Nanogold. *ACS Catal.* **2015**, *5* (7), 4385−4393.
(75) Laranjeira, J. A. S.; Fabris, G. S. L.; Ferrer, M. M.; Albuquerque, A. R.; Sambrano, J. R. Morphological Transformation Network of Nanoparticles via DFT Simulations. *Cryst. Growth Des.* **2020**, *20* (7), 4600−4611.
(76) Choudhury, B.; Choudhury, A. Ce^{3+} and Oxygen Vacancy Mediated Tuning of Structural and Optical Properties of CeO_2 Nanoparticles. *Mater. Chem. Phys.* **2012**, *131* (3), 666−671.
(77) Radović, M.; Stojadinović, B.; Tomić, N.; Golubović, A.; Matović, B.; Veljković, I.; Dohcević-Mitrović, Z. Investigation of Surface Defect States in CeO_{2-y} Nanocrystals by Scanning−tunneling Microscopy/Spectroscopy and Ellipsometry. *J. Appl. Phys.* **2014**, *116* (23), No. 234305.
(78) Malleshappa, J.; Nagabhushana, H.; Prasad, B. D.; Sharma, S. C.; Vidya, Y. S.; Anantharaju, K. S. Structural, Photoluminescence and Thermoluminescence Properties of CeO_2 Nanoparticles. *Optik* **2016**, *127* (2), 855−861.
(79) Aškrabić, S.; Dohčević-Mitrović, Z. D.; Araújo, V. D.; Ionita, G.; De Lima, M. M.; Cantarero, A. F-Centre Luminescence in Nanocrystalline CeO2. *J. Phys. D: Appl. Phys.* **2013**, *46* (49), No. 495306.
(80) Baur, F.; Jüstel, T. Eu^{3+} Activated Molybdates − Structure Property Relations. *Opt. Mater.: X* **2019**, *1*, No. 100015.
(81) Binnemans, K. Interpretation of Europium(III) Spectra. *Coord. Chem. Rev.* **2015**, *295*, 1−45.
(82) Liu, X.; Chen, S.; Wang, X. Synthesis and Photoluminescence of CeO_2:Eu^{3+} Phosphor Powders. *J. Lumin.* **2007**, *127* (2), 650−654.
(83) Tanner, P. A. Some Misconceptions Concerning the Electronic Spectra of Tri-Positive Europium and Cerium. *Chem. Soc. Rev.* **2013**, *42* (12), 5090−5101.
(84) Park, J. H.; Lim, Y. T.; Park, O. O.; Kim, J. K.; Yu, J. W.; Kim, Y. C. Polymer/Gold Nanoparticle Nanocomposite Light-Emitting Diodes: Enhancement of Electroluminescence Stability and Quantum Efficiency of Blue-Light-Emitting Polymers. *Chem. Mater.* **2004**, *16* (4), 688−692.
(85) Han, Y.; Gao, C.; Wang, Y.; Ju, D.; Zhou, A.; Song, F.; Huang, L.; Huang, W. Spatially Confined Luminescence Process in Tip-Modified Heterogeneous-Structured Microrods for High-Level Anti-Counterfeiting. *Phys. Chem. Chem. Phys.* **2018**, *20* (14), 9516−9522.
(86) Pazik, R.; Seisenbaeva, G. A.; Wiglusz, R. J.; Kepinski, L.; Kessler, V. G. Crystal Structure and Morphology Evolution in the $LaXO_3$, X = Al, Ga, in Nano-Oxide Series. Consequences for the Synthesis of Luminescent Phosphors. *Inorg. Chem.* **2011**, *50* (7), 2966−2974.
(87) Vimal, G.; Mani, K. P.; Biju, P. R.; Joseph, C.; Unnikrishnan, N. V.; Ittyachen, M. A. Structural Studies and Luminescence Properties of CeO_2:Eu^{3+} Nanophosphors Synthesized by Oxalate Precursor Method. *Appl. Nanosci.* **2015**, *5* (7), 837−846.
(88) Fröbel, M.; Fries, F.; Schwab, T.; Lenk, S.; Leo, K.; Gather, M. C.; Reineke, S. Three-Terminal RGB Full-Color OLED Pixels for Ultrahigh Density Displays. *Sci. Rep.* **2018**, *8*, No. 9684.
(89) Singh, R. K.; Som, S.; Lu, C. H. Spectroscopic Investigation of Red Eu^{3+} Doped Ceria Nanophosphors and Promising Color Rendition for Warm White LEDs. *J. Alloys Compd.* **2020**, *816*, No. 152653.
(90) Avram, D.; Rotaru, C.; Cojocaru, B.; Sanchez-Dominiguez, M.; Florea, M.; Tiseanu, C. Heavily Impregnated Ceria Nanoparticles with Europium Oxide: Spectroscopic Evidences for Homogenous Solid Solutions and Intrinsic Structure of Eu^{3+}-Oxygen Environments. *J. Mater. Sci.* **2014**, *49* (5), 2117−2126.
(91) Tiseanu, C.; Parvulescu, V. I.; Sanchez-Dominguez, M.; Boutonnet, M. Temperature Induced Conversion from Surface to Bulk Sites in Eu3-Impregnated CeO_2 Nanocrystals. *J. Appl. Phys.* **2012**, *112* (1), No. 013521.
(92) Primus, P. A.; Ritschel, T.; Sigüenza, P. Y.; Cauqui, M. A.; Hernández-Garrido, J. C.; Kumke, M. U. High-Resolution Spectroscopy of Europium-Doped Ceria as a Tool to Correlate Structure and Catalytic Activity. *J. Phys. Chem. C* **2014**, *118* (40), 23349−23360.

https://doi.org/10.1021/acsanm.4c00875
ACS Appl. Nano Mater. 2024, 7, 12466−12479